Journal of Cleaner Production 440 (2024) 141012

Contents lists available at ScienceDirect

Journal of Cleaner Production

journal homepage: www.elsevier.com/locate/jclepro

Solution-driven processing of calcium sulfate: The mechanism of the reversible transformation of gypsum to bassanite in brines

Tomasz M. Stawski [a,*], Stephanos Karafiludis [a,b,1], Carlos Pimentel [c,1], German Montes-Hernández [c], Zdravko Kochovski [d], Ralf Bienert [a], Karin Weimann [a], Franziska Emmerling [a,b], Ernesto Scoppola [e], Alexander E.S. Van Driessche [f,**]

[a] Federal Institute for Materials Research and Testing (BAM), Richard-Willstätter-Straße 11, 12489, Berlin, Germany
[b] Department of Chemistry, Humboldt-Universität zu Berlin, Brook-Taylor-Straße 2, 12489, Berlin, Germany
[c] Univ. Grenoble Alpes, Univ. Savoie Mont Blanc, CNRS, IRD, Univ. Gustave Eiffel, ISTerre, 38000, Grenoble, France
[d] Helmholtz-Zentrum Berlin for Materials and Energy, Hahn-Meitner Platz 1, 14109, Berlin, Germany
[e] Biomaterials, Hierarchical Structure of Biological and Bio-inspired Materials, Max Planck Institute of Colloids and Interfaces, Potsdam, 14476, Germany
[f] Instituto Andaluz de Ciencias de la Tierra (IACT), CSIC – Universidad de Granada, Av. De las Palmeras 4, 18100, Armilla, Spain

ARTICLE INFO

Handling Editor: Zhen Leng

Keywords:
Gypsum
Bassanite
Calcium sulfate
Brines
Transformation
Scattering
Synchrotron
Raman spectroscopy
Nucleation

ABSTRACT

Here, we show that calcium sulfate dihydrate (gypsum) can be directly, rapidly and reversibly converted to calcium sulfate hemihydrate (bassanite) in high salinity solutions (brines). The optimum conditions for the efficient production of bassanite in a short time (<5 min) involve the use of brines with c(NaCl) > 4 M and maintaining a temperature, T > 80 °C. When the solution containing bassanite crystals is cooled down to around room temperature, eventually gypsum is formed. When the temperature is raised again to T > 80 °C, bassanite is rapidly re-precipitated. This contrasts with the better-known behaviour of the bassanite phase in low-salt environments. In low-salinity aqueous solutions, bassanite is considered to be metastable with respect to gypsum and anhydrite, and therefore gypsum-to-bassanite conversion does not occur in pure water. Interestingly, the high-salinity transformation of gypsum-to-bassanite has been reported by many authors and used in practice for several decades, although its very occurrence actually contradicts numerical thermodynamic predictions regarding solubility of calcium sulfate phases. By following the evolution of crystalline phases with in situ and time-resolved X-ray diffraction/scattering and Raman spectroscopy, we demonstrated that the phase stability in brines at elevated temperatures was inaccurately represented in the thermodynamic databases. Most notably for c(NaCl) > 4 M, and T > 80 °C gypsum becomes readily more soluble than bassanite, which induces the direct precipitation of the latter from gypsum. The fact that these transformations are controlled by the solution provides extensive opportunities for precise manipulation of crystal formation. Our experiments confirmed that bassanite remained the sole crystalline phase for many hours before reverting into gypsum. This property is extremely advantageous for practical processing and efficient crystal extraction in industrial scenarios.

1. Introduction

Calcium sulfate hemihydrate ($CaSO_4 \cdot 0.5H_2O$), also known as bassanite, has been used as a precursor to produce gypsum (dihydrate, $CaSO_4 \cdot 2H_2O$) for various construction and decorative purposes since prehistoric times(Van Driessche et al., 2019). Nowadays, it is widely used for plasterboard and stucco manufacturing, construction, fire-proofing, biomedical applications, and even some forms of 3D printing. It is estimated that 100–200 million tonnes are used each year (Alyousef et al., 2023; Ash, 2019; Herrero et al., 2013; Weiss and Bräu, 2009), making it one of the most widely consumed mineral resources. However, as there are no significant natural deposits of bassanite existing on the Earth's surface, it has to be synthesized. The main route to obtain hemihydrate is a thermal treatment of gypsum at temperatures

* Corresponding author.
** Corresponding author.
E-mail addresses: tomasz.stawski@bam.de (T.M. Stawski), alexander.vd@csic.es (A.E.S. Van Driessche).
[1] These authors contributed equally.

https://doi.org/10.1016/j.jclepro.2024.141012
Received 4 October 2023; Received in revised form 5 January 2024; Accepted 28 January 2024
Available online 29 January 2024

typically between 150 °C and 200 °C to remove some of the structural water(Singh and Middendorf, 2007a). Depending on the method used, α- or β-hemihydrates are obtained either in humid/wet conditions or in dry air. Both types of hemihydrate will revert to gypsum when in contact with water, undergoing an exothermic hydration process that leads to the setting and hardening of the final gypsum-based material(La Bella et al., 2023). α- and β-hemihydrates differ in reactivity due to different crystal morphologies and structural defects, but whether they have the same crystal structure is still debated(Bezou et al., 1995; La Bella et al., 2023; Schmid et al., 2020). From an economic point of view, it is important to achieve hemihydrate synthesis in the shortest possible time with the lowest possible energy input is important since the mining of the raw material, gypsum, is relatively inexpensive and the energy expenditure is a significant portion of the synthesis or processing (Bouargane et al., 2023; Buchert et al., 2017; Gürtürk and Oztop, 2016). If dehydration is carried out in kilns and the energy is produced from fossil fuels, the environmental costs are particularly high. Using solar energy to dehydrate gypsum to produce β-hemihydrate is one way to improve the carbon footprint(López-Delgado et al., 2014; Salman and Khraishi, 1988). Alternatively, α-hemihydrate is produced from gypsum using an autoclave process(Guan et al., 2021). The widespread use and growing demand for calcium sulfates has led to the recognition that in some geographical regions, including the EU, calcium sulfate will be classified as a critical raw material within the next decade("European Commission - Gypsum industry news from Global Gypsum," n.d.; Haneklaus et al., 2022). Therefore, the search for alternative, more sustainable synthesis routes, which are not based on raw natural gypsum, and instead include calcium sulfate from waste, is of particular importance(Buchert et al., 2017; Weimann et al., 2021). Furthermore, considering the environmental impacts and monetary costs of gypsum disposal, targeted processing of calcium sulfate waste is crucial(Weimann et al., 2021).

Over the past decade, several alternative approaches have been explored to overcome the high-energy consumption of dehydration and the unfavourable continuous operation of the autoclave process to produce calcium sulfate hemihydrate at lower temperatures with reduced waste heat. Many of these methods are based on "wet" dehydration of gypsum or direct precipitation from mixed solutions containing calcium and sulfate, combined with a mixture of salt or acid (Guan et al., 2009a, 2023; Powell, 1962; Ru et al., 2012; Shen et al., 2020), alcohol/water(Guan et al., 2011; Tritschler et al., 2015a), and additives(Feldmann and Demopoulos, 2013; Reigl et al., 2023a, 2023b). Other approaches include solvent-assisted grinding of gypsum(Maslyk et al., 2022) and a solvothermal route using amorphous Ca-ethoxide as a precursor(Burgos-Ruiz et al., 2021). While some of these methods show promise in reducing energy consumption and waste heat, they often rely on expensive additives, the use of large quantities of organic solvents or the need for extensive milling times. These factors limit their widespread application in industrial settings. Therefore, further research is warranted to find alternative approaches that strike a balance between efficiency, cost-effectiveness, and environmental sustainability in the production of calcium sulfate hemihydrate on a larger scale. These hurdles have stimulated the development of a solution-based processing method for gypsum using hyper-saline brines(Ding et al., 2023; Nie et al., 2023; Powell, 1962; Reiss et al., 2021; Ru et al., 2012), as a simple yet effective way to control the stability ranges of the different calcium sulfate phases. We demonstrate that in (hypersaline, >4 M) brines, it is possible to produce calcium sulfate hemihydrate in a rapid and cyclic manner. The major advantage of this method, compared to solid state and autoclave methods, is that all the transformations take place in an aqueous medium at temperatures well below the boiling point of water (Bouargane et al., 2023). Liquid water solutions inherently have a high heat capacity, which can help reduce energy losses during the bassanite synthesis processes. By using insulated, closed-loop reactors, we can further improve energy efficiency and optimize the production of calcium sulfate hemihydrate, making the process even more attractive from an economic and environmental perspective.

Bassanite is considered to be metastable in solution with respect to gypsum and anhydrite(Van Driessche et al., 2019) (Fig. 1A). This explains why bassanite deposits do not persist on Earth, except in extreme arid areas, such as the desert of Atacama or volcanic deposits(Van Driessche et al., 2019). However, experimental observations indicate that the persistence of bassanite is dramatically increased in solution with high ionic strength(Nie et al., 2023), the fact of which has been used to produce bassanite(Ding et al., 2023; Guan et al., 2023; Ru et al., 2012). Yet, when looking at the solubility of the different $CaSO_4$ phases in a concentrated NaCl solution the stability region of bassanite is not expected (and sometimes even not observed(He et al., 1994)). The problem mainly lies in the quality of the thermodynamic data. In Fig. 1B we show solubility curves of the three calcium sulfate phases calculated using the widely used geochemical modelling software PHREEQC 2 (Parkhurst and Appelo, 1999) and the included Pitzer database (see also SI: Materials and Methods). According to this calculation, in hypersaline brines (in our case 4.8 M, see SI: Materials and Methods), the transition point between gypsum and anhydrite is shifted to a temperature of $T < 30$ °C, but bassanite supposedly remains metastable for the entire temperature range. Thus, bassanite should not form from solution under these conditions, which is incorrect.

However, it is important to note that these curves are merely extrapolations from experimental data, where the solubility of $CaSO_4$ phases in high salinity solutions has been mainly determined experimentally for some temperature ranges. This becomes apparent when the solubility curves (Fig. 1C) are calculated using the latest version of PHREEQC 3(Parkhurst and Appelo, 2013) with an updated Pitzer database (SI: Methods, Eq. S1, Table S1). Updated and improved data suggest that bassanite does become the stable phase at $T > \sim 110$ °C in 4.8 M brines. This would explain the experimental observation that bassanite forms at this temperature in high salinity experiments(Guan et al., 2023; Ru et al., 2012; Zürz et al., 1991), but it contradicts the observation that anhydrite should eventually form at these conditions (Fig. 1D and ref(Ossorio et al., 2014).). These uncertainties regarding the phase diagram of $CaSO_4$ have hampered the search for a large-scale synthesis route for bassanite at a lower temperature, and thus lower environmental cost.

Here, guided by our previous experimental results, solubility calculations (Fig. 1B and C) and other studies(Aagli et al., 2005; Ding et al., 2023; Fu et al., 2012; Guan et al., 2009a, 2023, 2021; Nie et al., 2023; Ru et al., 2012; Zürz et al., 1991) we preselected an optimal window, indicated by the red rectangle Fig. 1C, to produce bassanite via a simple and efficient cyclic synthesis method. Although various thermodynamic and applied aspects of this brine solution method have been reported in the literature(Guan et al., 2009a, 2011; Gürtürk and Oztop, 2016; Salman and Khraishi, 1988; Tritschler et al., 2015b), the actual conversion of gypsum to bassanite in brines has not been so far explored from the perspective of nano-scale mechanisms, which will be discussed in detail in the next sections.

2. Materials and Methods

In our experiments, we followed the phase changes occurring in a solution containing 0.2 M $CaSO_4$ and 4.8 M NaCl. The detailed description of the synthesis and characterisation methods is presented in the SI: Materials and Methods. This choice of solution conditions was based on our previous work, in which we found that bassanite precipitated directly at $T > 80$ °C, while at $T < 80$ °C only gypsum was observed (Ossorio et al., 2014; Stawski et al., 2020). Taking into account the updated solubility calculations (Fig. 1C) and our previous experimental results (Fig, 1D), we selected a narrow window of temperatures, around $T = 90$ °C, to evaluate the stability of calcium sulfate phases, which was done by performing in situ and time-resolved X-ray scattering/diffraction (Fig. 2, Fig. 3A) and Raman spectroscopy (Fig. 3B, Fig. S2).

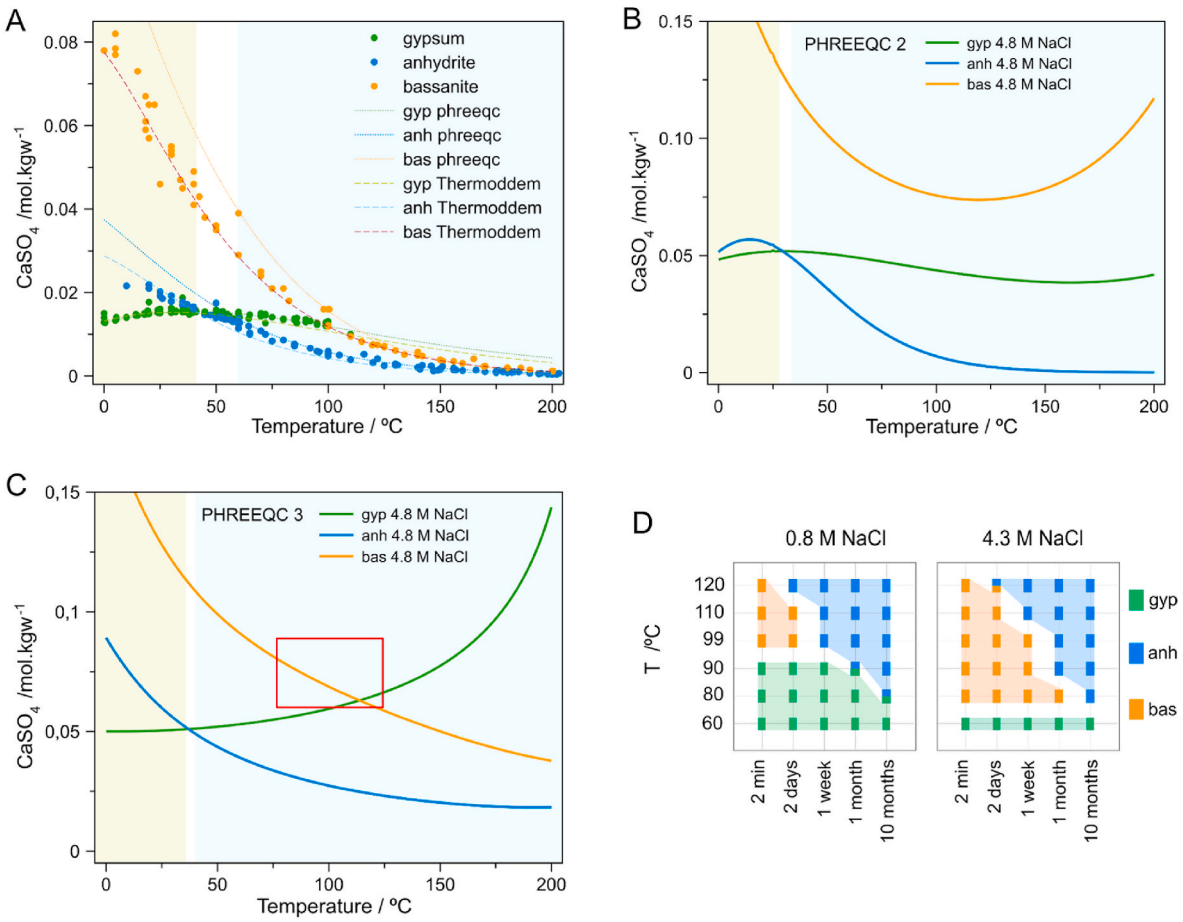

Fig. 1. (A) Phase diagram of $CaSO_4$–H_2O, including the solubility curves for gypsum, anhydrite and bassanite in pure water as a function of temperature. The plot contains experimental data extracted from literature (dots) and curves calculated with PHREEQC 2 (dotted lines) and thermoddem.V1 (stripe lines) databases. Shaded areas indicate the stability regions of gypsum (light green) and anhydrite (light blue). The white area between the phase stability regions indicates the uncertainty in the transition temperature between both phases. (B) Phase diagram of $CaSO_4$–H_2O in the presence of 4.8 M NaCl calculated using PHREEQC 2.; (C) Phase diagram of $CaSO_4$–H_2O in the presence of 4.8 M NaCl calculated using PHREEQC 3. The red square indicates the selected window to synthesize bassanite; (D) The main $CaSO_4$ phase(s) obtained by direct precipitation as a function of time, salinity, and temperature. Experiments at T = 60 °C were monitored for up to two years of reaction time, but the precipitate remained phase-pure gypsum (adapted from Ossorio et al., 2014; Ossorio et al., 2014)). (For interpretation of the references to colour in this figure legend, the reader is referred to the Web version of this article.)

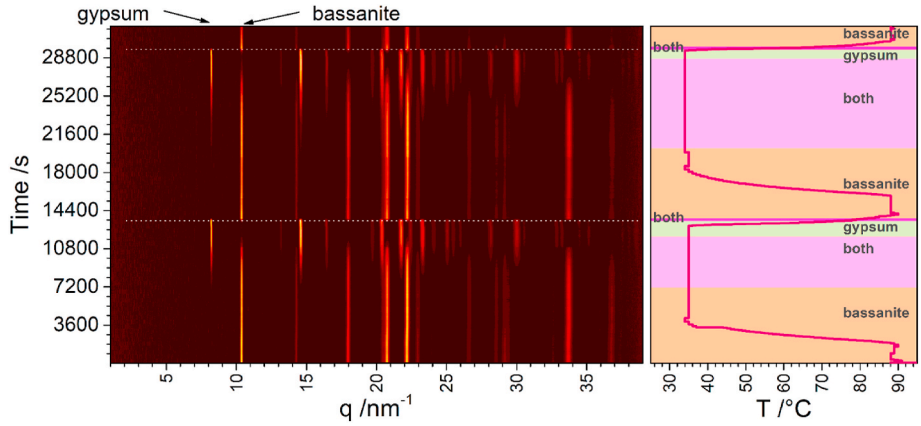

Fig. 2. Time-resolved crystalline phase transformations in calcium sulfate system under cyclic temperature profile. (left) The in situ and time-resolved isotropic diffractogram showing crystalline phases which form in a 0.2 M $CaSO_4$ - 4.8M NaCl aqueous solution upon following a cyclic temperature profile (right) over a period of ~9 h. The first characteristic peaks of gypsum (COD 2300259) and bassanite (AMCSD 0006909) are indicated with arrows. The coloured backgrounds: gypsum (green), bassanite (orange); both phases (purple). (For interpretation of the references to colour in this figure legend, the reader is referred to the Web version of this article.)

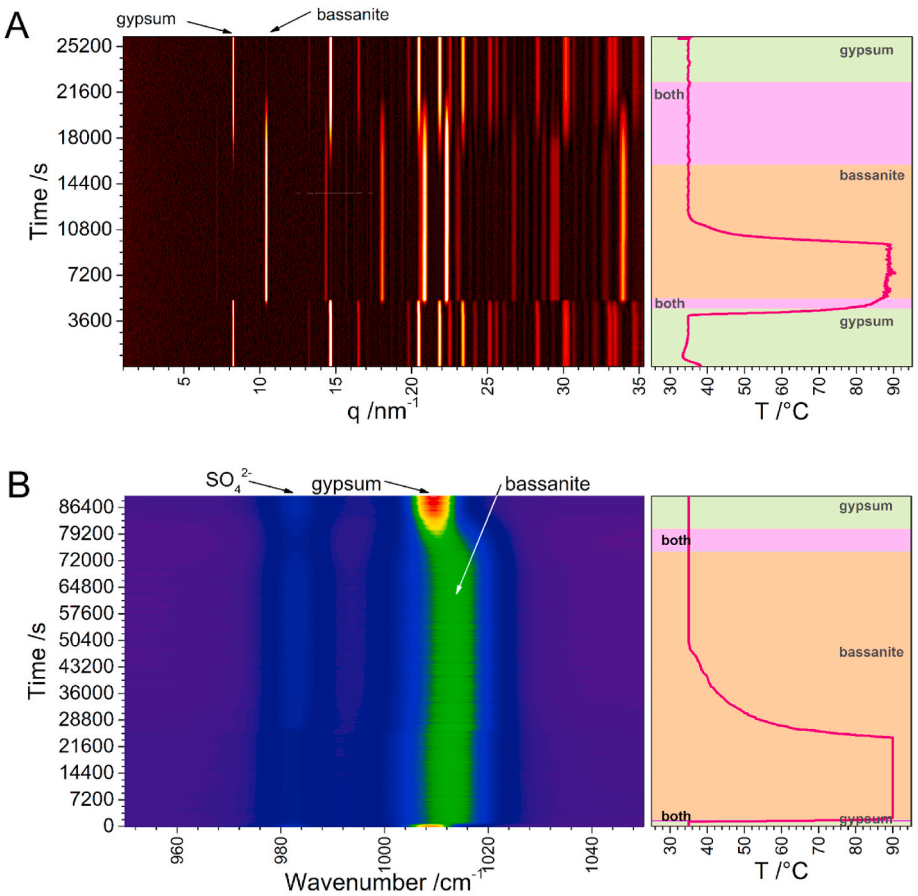

Fig. 3. In situ time-resolved characterization of calcium sulfate phase transformations A) (left) In situ and time-resolved isotropic diffractogram showing the crystalline phases that form in a 0.2 M $CaSO_4$ - 4.8 M NaCl solution while following a temperature profile (right). The first characteristic peaks of gypsum (COD 2300259) and bassanite (AMCSD 0006909) are indicated with arrows. B) (left) In situ time-resolved Raman spectroscopy of the gypsum to bassanite to gypsum conversion in 4.8 M NaCl following a temperature profile (right). Gypsum precipitated at T = 35 °C from a solution containing 0.2 M $CaSO_4$ and 4.8 M NaCl rapidly (<420 s) started to transform into bassanite when the temperature was increased to T = 90 °C. This is highlighted by a shift in the v1 mode band from 1008 cm^{-1} to 1016 cm^{-1}. When the temperature is lowered again to T = 35 °C, bassanite slowly converts back into gypsum after a long induction time (~45000 s). The coloured backgrounds: gypsum (green), bassanite (orange); both phases (purple). (For interpretation of the references to colour in this figure legend, the reader is referred to the Web version of this article.)

3. Results and discussion

3.1. Cyclic transformation of gypsum to bassanite

We monitored precipitation from a solution containing 0.2 M $CaSO_4$ and 4.8 M NaCl at 90 °C using in situ scattering (Fig. 2). In this scenario, bassanite formed rapidly as the only crystalline phase. Subsequently, the solution was cooled down to T = 35 °C, which eventually induced the precipitation of gypsum. However, at this temperature the gypsum phase had started to form only after an extensive induction time of ~4800 s, and both phases still coexisted for the following 3600 s. This pointed to very slow kinetics of the hydration of bassanite to gypsum, thus explaining its persistence under high-salinity conditions. This stands in opposition to the typical behaviour of this phase in low salt environments, where a short induction time and rapid transformation is typically reported(Singh and Middendorf, 2007b). On the other hand, increasing the temperature to T = 90 °C (>13000 s), resulted in an almost instantaneous (<300 s) reconversion of gypsum into bassanite. These cycles were repeated several times, showing a similar duration of the different phase transformations (Fig. 2), thus demonstrating the full reversibility of the process.

Surprisingly, this temperature-dependent cyclic phase change confirms a range of physicochemical conditions where bassanite is thermodynamically more stable than gypsum. Additionally, it also shows that the formation of anhydrite, the $CaSO_4$ phase with the lowest solubility is kinetically hindered at T = 90 °C, (Ossorio et al., 2014). Importantly, the almost instantaneous gypsum-bassanite conversion occurs at a distinct temperature boundary. In a different variant of our scattering experiment, we precipitated gypsum at T = 35 °C and heated this slurry in 5 °C increments up to T = 90 °C, with each temperature being maintained for 900 s (15 min) (SI: Fig. S1). The scattering data revealed that the rapid transition is viable only at a threshold temperature of T = 80 °C, which is significantly lower than the one predicted by the solubility calculations shown in Fig. 1C (T = ~110 °C). Furthermore, in static experiments (i.e. without stirring), we obtained bassanite at T = 70 °C after 5 days (SI: Table S1). Overall, these observations contradict the calculated solubility data shown in Fig. 1A and B, but they do confirm the previously reported stability behaviour of the calcium sulfate phases precipitating from brines solutions shown in Fig. 1C.

We further focused experimentally on a single cycle of gypsum-bassanite-gypsum conversion with extended reaction times for 35 °C < T < 90 °C (>25000 s with scattering and >70000 s with Raman spectroscopy, Fig. 3). With these measurements, we intended to exclude a possibility that the occurrence of the cyclic transformations is driven by the residual seeds of the bassanite phase. Such seeds, hypothetically, might nucleate the hemihydrate phase, although it would be thermodynamically unfavourable(Bučar et al., 2015; Dunitz and Bernstein, 1995). To fully exclude this scenario in Fig. 3, the experiments start with

gypsum. Moreover, the equilibration periods, when only gypsum exists, are extended with respect to Fig. 2, to further ensure that no trace bassanite is present. In these experiments, we also observed the rapid transformation of gypsum to bassanite upon heating the solution to T = 90 °C, followed by the slow conversion of bassanite back to gypsum upon cooling to T = 35 °C. These observed trends are fully consistent with those depicted in Fig. 2. Hence, the transformation relies on the specific temperature threshold. Moreover, independent in situ Raman spectroscopy monitoring (Fig. 3B; Fig. S2) of two gypsum-bassanite-gypsum conversion cycles revealed the same trends. However, in Raman, the conversion of bassanite to gypsum was notably slower, with bassanite persisting for an extended period (~51000 s) after the solution commenced to cool down to T = 35 °C (T < 90 °C at ~24000 s, T = 35 °C at ~47000 s). Bassanite started to convert to gypsum at ~75000 s. The longer persistence of bassanite in the in situ Raman experiment compared to the in situ scattering experiment is most likely the result of the inherent differences in the hydrodynamic regimes between both setups(Karafiludis et al., 2023; Montes-Hernandez and Renard, 2016). In the latter, the solution was vigorously stirred (1000 rpm) in the reactor vessel and continuously recirculated through a capillary using a peristaltic pump. In contrast, the Raman setup involved gentler stirring (400 rpm) of the solution in the reaction vessel. The impact of the hydrodynamic regime on the transformation kinetics is further supported by a series of experiments conducted without stirring, where the conversion kinetics are indeed further slowed down (SI: Table S2).

3.2. *Mechanism of cyclic conversion – structural changes –*

The scattering data contain a plethora of information regarding phase, morphology, and size evolution during the transformation reactions because we measured a continuous, gapless signal for 0.1 nm^{-1} < q < 35 nm^{-1}. Based on this data, we elucidated the structural changes taking place during the conversion reaction. We analysed changes in the orientation-dependent anisotropic 2D intensity profiles (SI: Fig. S3, Fig. S4). The rationale and the details of the analyses are included in the SI: Materials and Methods.

In Fig. 4A we present the evolution of peak areas from the reflections at q_{bass}~ 10.42 nm^{-1}, characteristic of bassanite (110), and q_{gyp} ~ 8.25 nm^{-1}, characteristic of gypsum (020), as shown in Fig. 3A. The trend, as a function of T and time, reveals changes in anisotropy as the crystalline phases evolve. Generally, an increase in anisotropy is correlated with larger crystal sizes and aspect ratios. Conversely, at T > 80 °C (>4800 s), the decrease in anisotropy indicates a dissolution-reprecipitation process, since it correlates with a decrease in the crystal size of gypsum and concurrent nucleation and subsequent growth of isotropic nano-sized bassanite crystals. This effect becomes evident through analysis of the changes in the ρ parameter, calculated from the pseudo-invariant expressing q^2-weighted integral intensity: $Q^* = \int_{q_{min}}^{q_{max}} q^2 I(q) dq$ (Fig. 4B) over our available q-range. We independently calculated the pseudo-invariant for the meridian and equatorial directions (SI: Fig. S3). The value $\rho = Q^*_{meridian}/Q^*_{equatorial}$ highlights that the nucleation of bassanite at T > 80 °C is associated with the formation of near-isotropic crystals/particles (ρ approaches 1). Conversely, the growth of larger crystals of any phase results in ρ deviating from 1, where ρ < 1 implies that crystals' long axes are aligned horizontally. Interestingly, after the formation of small isotropic bassanite particles, upon cooling to T = 35 °C, this phase continues to grow, becoming more anisotropic. This is evidenced by the sharp drop in ρ after ~9600 s. Gypsum does not appear in diffraction until ~15900 s. This extended growth period of bassanite outside its stability window (Fig. 1C) offers the possibility to convert gypsum to phase-pure bassanite with specific sizes/morphologies. Our small-angle data analysis further supports this notion (SI: Materials and Methods). In this regard, morphologically, the early-stage bassanite would be more similar to the β-hemihydrate form (i.e. small size and high surface area), while the developed crystals would be α-hemihydrate (i.e. large idiomorphic crystals), as has been reported by other authors. (Guan et al., 2011, 2023; Ru et al., 2012).

The morphological and size-distribution changes of the crystals during the gypsum-bassanite phase transformation (Figs. 3 and 4) are also evident at low-angles (SI: Fig. S4, Fig. 5). In Fig. 5A, we present small-angle scattering data from three characteristic moments: 3200 s

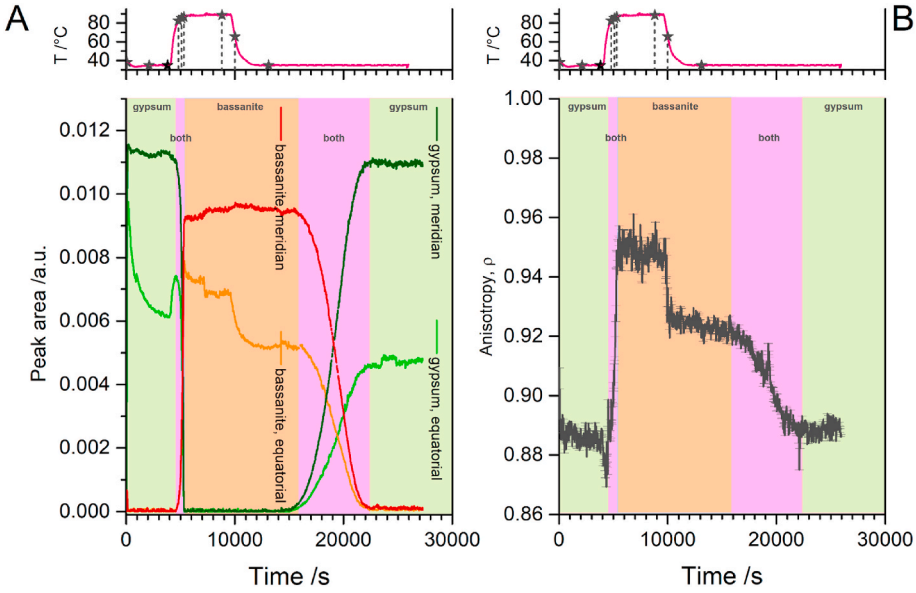

Fig. 4. Anisotropy evolution and phase changes in calcium sulfate crystals during transformation reactions. A) Changes in the peak areas q_{bass}~ 10.42 nm^{-1} for bassanite (110, orange) and q_{gyp} ~ 8.25 nm^{-1} for gypsum (green, 020); the curves show independently for gypsum (shades of green) and bassanite (shades of orange) the changes for the meridian and equatorial integrations; B) the evolution of an anisotropy parameter ρ = ; the temperature profile (top) is included for each data set, and the time axes are matching. Characteristic time points marking the changes in anisotropy and the evolution of crystalline phases, corresponding to the frames in Fig. S3, are marked with stars. The coloured backgrounds: gypsum (green), bassanite (orange); both phases (purple). (For interpretation of the references to colour in this figure legend, the reader is referred to the Web version of this article.)

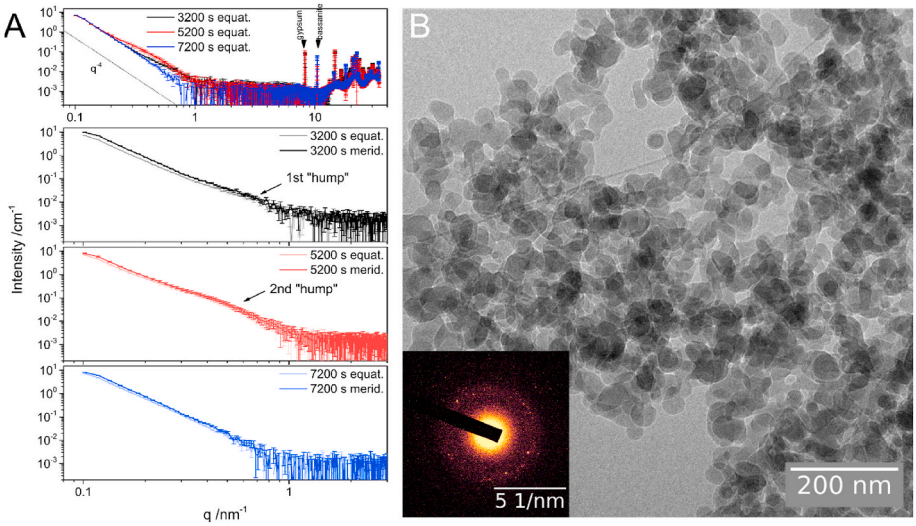

Fig. 5. A) Selected small-angle scattering curves from developed gypsum crystals at T = 35 °C (3200 s); gypsum-bassanite transformation at T = 90 °C (5200 s); developed bassanite crystals at T = 90 °C. The small-angle region $q < 3$ nm^{-1} compares the meridian and equatorial intensities, as they involve for the three considered cases; B) cryo-TEM image which corresponds roughly to scattering at ~5200 s, and shows the presence of bassanite nanocrystals, as is confirmed by the electron diffraction (inset).

when only well-developed gypsum is present at T = 35 °C; 5200 s, which marks the crossover between the dissolution of gypsum and the formation of bassanite; and 7200 s when bassanite exists at T = 90 °C. Our minimum q was limited to 0.1 nm^{-1}, which corresponds to a maximum feature size of ~60 nm. However, gypsum and bassanite crystals typically grow to many microns in size and beyond(Stawski et al., 2019), and therefore, we observe them in scattering predominantly as Porod interfaces following approximately an $I(q) \propto q^{-4}$ dependence(Besselink et al., 2016; Stawski et al., 2016, 2020) (dashed line in Fig. 5A). Such an interface is observed in all the curves for at least $q <$ ~0.3 nm^{-1}, indicating that larger crystals are always present. A comparison of scattering features from 3200 s (53.3 min) and 7200 s, i.e., pure gypsum vs. bassanite, reveals that the initially precipitated gypsum crystals from the first cycle (Fig. 3A) exhibit a deviation from a Porod interface at q ~0.7 nm^{-1} (i.e., the 1st small "hump"-like deviation, Fig. 5A). The profile is anisotropic (SI: Fig. S4) and implies the presence of oriented scattering features of ~10 nm in size, confirming the mesostructured nature of gypsum crystals(Besselink et al., 2016; Stawski et al., 2019). Noteworthy, these oriented nano-features partially disappear in developed bassanite crystals after 7200 s and in the re-precipitated gypsum after 15900 s (Fig. 3).

A critical moment in the transformation of gypsum to bassanite occurs at ~4860 s, marked by the appearance of a 2nd “hump” with a centroid at q ~0.5 nm^{-1} (compare 3200 s vs. 5200 s in Fig. 5A). The isotropic character and slight shift in q of this feature indicate the formation of small particles independently of the oriented ones (the 1st hump) already present in the crystals. This supports the notion of the *de novo* nucleation of bassanite. In Fig. 5B, a cryo-TEM image captured as close as possible after the onset of the gypsum-bassanite transformation (corresponding to ~4860–5200 s in Fig. 4A) depicts aggregates of polydisperse crystalline nanoparticles of bassanite (electron diffraction, inset in Fig. 5B), with the smallest particles measuring around 10 nm in diameter. Such nano-crystals would be classified as β-hemihydrate.

We further quantified the evolution in the small-angle scattering patterns by independently fitting the data using Eq. S3 (SI: Materials and Methods, and SI: Fig. S5) for both the meridian- and equatorial-integrated curves. The trends, summarised in Fig. 6, provide additional insights into the mechanism of the transformations, including the presence of mesocrystallinity. These trends capture comprehensive structural features for q < 3 nm^{-1} and are not specific to any particular phase. However, when correlated with the diffraction peaks (Figs. 3A and 4A), we can easily attribute the observed changes to the evolution of crystalline phases. In Fig. 7, we present a schematic illustration of the concepts resulting from the observed trends.

In Fig. 6, the parameter B, in general, is proportional to a specific surface of the solid phases when $D > 3$ (i.e. surface fractals, SI: Eq. S3). Initially, as gypsum crystals grow before ~4000 s (T = 35 °C), this parameter gradually decreases in both directions due to a reduction in surface-to-volume ratio. The decrease in surface-to-volume ratio suggests the development of larger crystals while smaller particles/crystals disappear, possibly through processes such as Ostwald ripening or coalescence(Conti et al., 2002), or the coalescence of the internal mesocrystalline domains(Stawski et al., 2019, 2021). Due to the shape of the crystals and their alignment, B evolves independently for the two integration directions. The difference between the two B values increases with time at constant T = 35 °C, indicating that aligned crystals are growing in length and increasing their aspect ratios. Interestingly, it appears that in situ precipitated gypsum crystals continuously undergo structural changes, reflected by the continuous decrease in B values, during the initial 4000 s (Fig. 7, stage I).

After ~4000 s, when T > 80 °C, the onset of gypsum dissolution leads to the formation of numerous small bassanite particles (Fig. 7, stages II and III). These two processes result in a peak in B at 4860 s (Figs. 6, 2–3 fold jump worth respect to ~4000 s). The system becomes briefly isotropic, due to the *de novo* nucleation of bassanite (see also Fig. 5B). The meridian and equatorial values of B overlap and gradually decrease until gypsum is fully dissolved at 5400 s. After 5400 s, at T = 90 °C, the anisotropy begins to develop, and the equatorial values of B sharply decrease, indicating the continued evolution of bassanite crystals (Fig. 7, stage II and III). By 9600 s, when T = 90 °C, the meridian and equatorial B values reach their plateaus. After 9600 s, as the temperature gradually decreases to T = 35 °C, the meridian B remains relatively constant. However, the equatorial counterpart continues to slowly and monotonously decrease by ~20%, around 12000 s. This observation aligns with the evolution of the diffraction peaks and the ρ parameter shown in Fig. 4, indicating a continuous increase in the aspect ratio of the bassanite crystals, which at this point might be classified as α-hemihydrate (Fig. 7, stage III). This can be attributed to the slow dissolution of bassanite crystals, strongly supported by our in situ Raman spectroscopy data, which we will further discuss.

After 15000 s, bassanite gradually starts its reconversion to gypsum (Fig. 6; Fig. 7, stage IV and V). This transformation is accompanied by a

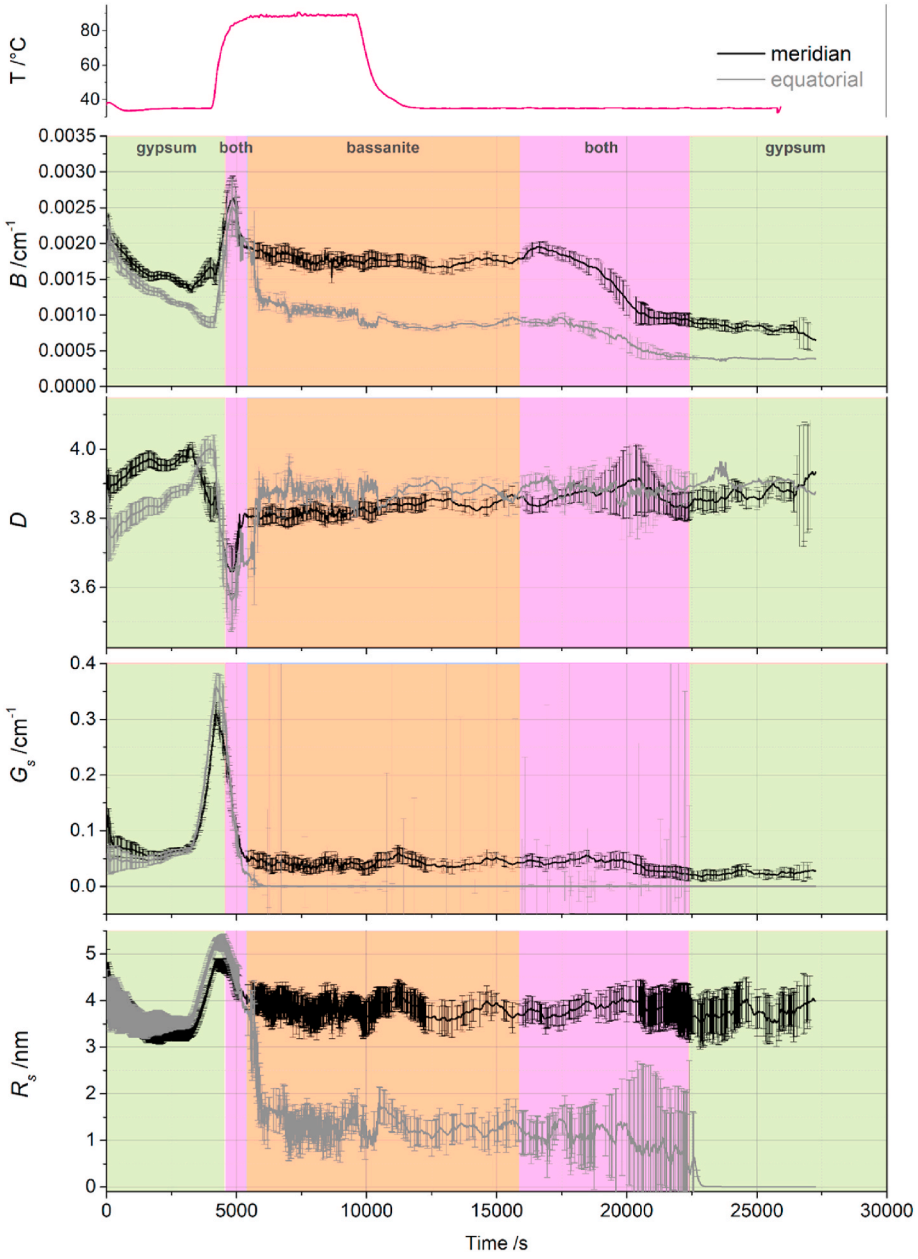

Fig. 6. The evolution of the fitting parameters derived for the model in Eq. S3, which characterise the small-angle scattering data. The temperature profile is included for reference. Independent trends for meridian (black) and equatorial directions (grey). The coloured backgrounds: gypsum (green), bassanite (orange); both phases (purple). *B* represents changes to a specific surface of the solid phases; *D* is a scattering exponent, which measures the evolution of the roughness of interfaces; G_s is proportional to the product of the volume fraction and the volume of smaller particles; R_s is the gyration radius of small structural units. In addition, Fig. S6 shows trends in B_s and *bkg* parameters. (For interpretation of the references to colour in this figure legend, the reader is referred to the Web version of this article.)

reduction in the surface-to-volume ratio in both the meridian and equatorial directions, leading to a decrease in the *B* parameter. This is because the crystals of both calcium sulfates change shape during the phase transition. Additionally, the re-precipitation of gypsum from bassanite after 15000 s is characterised by overall lower *B* values compared to the initial gypsum formed before 4000 s. This suggests that these two entities of gypsum have different crystal size distributions and (meso)structures, as we infer from other trends observed in Fig. 6.

The changes in exponent *D* (Fig. 6) represent the evolution of interface roughness and the presence of surface fractals(Besselink et al., 2016). These interfaces originate from large crystals "outside" our *q*-range. Smooth Porod interfaces exhibit $D = 4$, while rougher surfaces have $3 < D < 4$, with lower *D* values indicating higher roughness(Besselink et al., 2016). Additionally, this parameter tracks the anisotropic evolution of crystals, where the roughness of the gypsum surface is direction-dependent before ~4000 s (T = 35 °C). This phenomenon further supports the mesocrystalline nature of freshly precipitated gypsum crystals(Stawski et al., 2021) (Fig. 7, stage I). The formation of bassanite nano-crystals leads to a decrease in *D* (Fig. 7, stage II), indicating an increase in roughness, which correlates with an increase in specific surface area as reflected by the spike in parameter *B*. Subsequently, the growth of larger bassanite crystals (>5400 s, Fig. 7, stage III) and their conversion to gypsum (>15000 s, Fig. 7, stages IV and V) results in smoother crystalline interfaces, with *D* values closer to 4. The meridian and equatorial directions also exhibit less divergence in their *D* values. The isotropic *D* values suggest that mesocrystallinity partially disappears in well-developed bassanite crystals and in gypsum formed through the hydration of bassanite at T = 35 °C. In this regard, the two

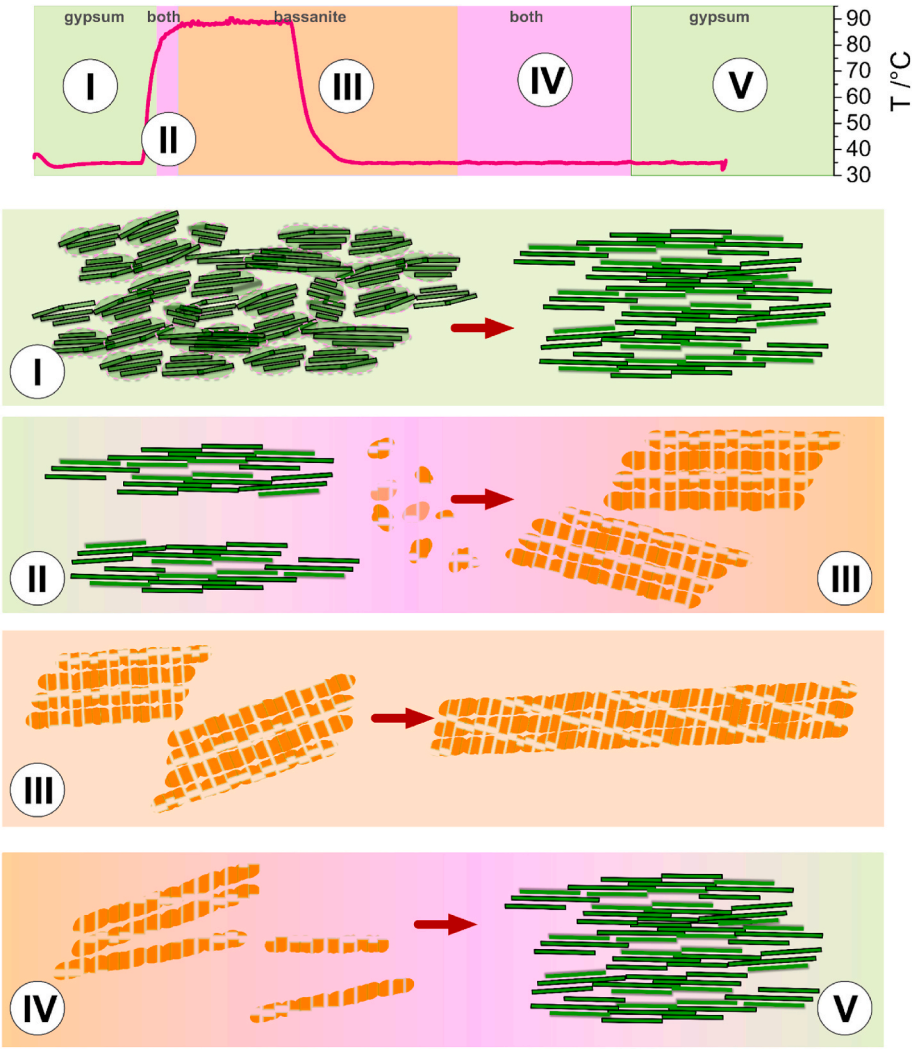

Fig. 7. Mechanisms involved in temperature-driven cyclic gypsum-bassanite transformations in hypersaline brines. The temperature profile is included (top). The coloured backgrounds mark: gypsum (green), bassanite (orange); both phases (purple). (I) Formation of gypsum. Gypsum crystals (green) which nucleate from a homogenous solution exhibit pronounced mesocrystalline disorder and continue to internally evolve, despite reaching a thermodynamic equilibrium; (II) - (III) upon reaching T > 80 °C, gypsum crystals (light red) rapidly dissolve, and bassanite nano-sized crystals (orange) are heterogeneously nucleated to grow (III) into larger micron-sized units. The resulting bassanite crystals show less pronounced mesocrystalline disorder than the original gypsum crystals (III) upon cooling to T ≪ 80 °C bassanite crystals partially dissolve, and increase their aspect ratio by growing in length and decreasing in width; (IV)-(V) after a long induction time bassanite dissolved and gypsum crystals form heterogeneously. The re-precipitated gypsum crystals show less pronounced mesocrystalline disorder than the original gypsum crystals from (I). (For interpretation of the references to colour in this figure legend, the reader is referred to the Web version of this article.)

occurrences of gypsum, before and after the heating step at T = 90 °C, again appear to have different mesostructures, as also indicated by parameter *B*. This distinction is further reflected in the trends observed in the R_s and G_s parameters.

In Eq. S3 (SI: Materials and Methods), the mentioned variables parameterize the Guinier form factor, which is used to approximate any small units that may exist within the crystals, such as "bricks-in-the-wall" or "loose" particles with radii of gyration R_s. Additionally, G_s is proportional to the product of the volume fraction and the volume of these smaller particles. The initial as-precipitated gypsum, before 4000 s, contains small building units with a radius of ~4 nm. We interpret these units as components of a mesocrystal, consistent with our previous work (Stawski et al., 2016) (Fig. 7, stage I). The dissolution of gypsum with increasing temperature induces the rapid formation of a large population of nanoparticles at 4860 s, causing the radius of gyration of the small units to increase to ~5.5 nm (Fig. 7, stage II). Further crystallization of bassanite results in a partial loss of the mesostructure. The constituent building blocks are only observable in the meridian direction (R_s ~ 4 nm), while they vanish in the equatorial direction, as indicated by $G_s \sim 0$ after 5400 s. This observation aligns with a decrease in the specific surface area expressed by parameter *B*, assuming crystal growth occurs through the coalescence of internal mesocrystal domains (Stawski et al., 2016). Examining the meridian and equatorial trends in Fig. 6, the surviving mesostructure indicates that the crystals possess domains with shorter, nano-sized features aligned parallel to the long axes (c-axes) of the crystals. Such alignment correlates with the layer structure of gypsum and the channel structure of bassanite, where these anisotropic motifs align parallel to the long axes of the respective crystals (Fig. 7). In the perpendicular directions, the domains fuse into a homogenous body, cancelling the mesostructure.

3.3. *Mechanism of conversion – solubility of calcium sulfate phases –*

The scattering data demonstrate that the initial gypsum crystals precipitated from stock solutions (Fig. 7, stage I) exhibit greater internal disorder compared to the stable bassanite crystals (Fig. 7, stage III). Importantly, this difference in the mesostructure is also observed for the re-precipitated gypsum crystals formed through the hydration of

bassanite (Fig. 7, stage V). The question now arises, how can we rationalise the occurrence of these different mesostructures? It is known that the hydration of bassanite to gypsum involves a dissolution-reprecipitation process in contrast to solid-state diffusion(Saha et al., 2012), which is seemingly also the case for our gypsum-bassanite transformation. When we compare the two gypsum formation events (Fig. 7), the first occurrence happens through mostly homogeneous nucleation upon mixing of the two stock solutions. However, all subsequent nucleation and crystallization events occur from heterogeneous solutions, as the growth of *de novo* crystalline phases occurs in the presence of dissolving preceding phase, and thus solid interfaces. This is the case for both bassanite and gypsum nucleation (Fig. 7, stages II-V). We propose that such heterogeneous surface-affected nucleation processes lead to the formation of less mesostructured crystals compared to those growing from homogeneous bulk solutions. Furthermore, as we discuss in the next section, the determined structural and morphological changes, as well as the structural disorder associated with phase transitions in brines, are driven by temperature-dependent changes in the solubility of bassanite and gypsum (Fig. 1C). These changes in solubility, in turn, control the rates of nucleation and crystal growth.

To specifically measure the solubility changes of calcium sulfate phases during temperature variations, we employed Raman spectroscopy to monitor the cyclic formation of gypsum and its subsequent transformation to bassanite (Fig. 3B, SI: Materials and Methods). Through the analysis of time-resolved Raman spectra, we were able to determine the variations in the concentration of dissolved "free" sulfate in the solution. This was achieved by tracking the peak of the $\nu 1$ mode of aqueous sulfate at ~980 cm^{-1} (Figs. 3B and 8).

Using our Raman setup we performed an experiment analogous to the one with scattering in Fig. 3A, in which after mixing the stock solutions of $CaCl_2$ and Na_2SO_4 (0.2 M $CaSO_4$ in 4.8 M NaCl), gypsum precipitated (Fig. 3B, Fig. S2). The time scales of the spectroscopic experiment differ from the scattering experiment due to specific constraints of each experimental setup (SI: Materials and Methods, Table S2). However, the essential aspects of the gypsum-bassanite transformations are analogous and directly comparable between the two approaches (Fig. 3). Upon the precipitation of gypsum, the sulfate concentration gradually decreased during the initial 1800 s to ~39 mM, after which it remained stable until the temperature was raised to T = 90 °C (Fig. 8A). The plateau in sulfate concentration at T = 35 °C indicated that the system had approached a state of thermodynamic equilibrium. However, from the scattering trends observed in Fig. 6, it is evident that gypsum crystals continued to evolve even before the temperature increase (Fig. 7, stage I).

Upon heating the system to T = 90 °C, we observed a significant increase in the concentration of free sulfate, reaching ~46 mM, due to the dissolution of gypsum (Fig. 8; Fig. 7, stage II), in agreement with the general solubility trend shown in Fig. 1C. As bassanite started to form after 61260 s (420 s relative to the increase in T), the sulfate concentration rapidly decreased within the first 480 s (relative) to ~37 mM, and no gypsum was detected anymore. This initial increase in sulfate concentration, followed by a drop during the gypsum-bassanite transformation, supports the hypothesis of transformation through dissolution-reprecipitation. It also correlates with the rapid nucleation of bassanite nanoparticles (Fig. 7, stage II). Nucleation is thus driven by a jump in saturation caused by the rapid dissolution of gypsum as it reaches its metastability region. From that point onward (61740 s), the sulfate concentration decreased further to ~26 mM at T = 90 °C.

As the solution started to cool down to T = 35 °C, bassanite began to dissolve, increasing the sulfate concentration to ~41 mM. After a prolonged induction time (relative ~48000 s), gypsum started to crystallize, causing the sulfate concentration to decrease to ~37 mM. These two reduction steps in sulfate concentration are consistent with our scattering data (Figs. 4, Figs. 5 and 6), where we observed the morphological evolution of bassanite crystals induced by cooling before any gypsum crystals appeared. In fact, this dissolution of bassanite accompanied by an increase in sulfate concentration, is analogous to the reverse gypsum-bassanite transformation. The key difference lies in the kinetic rates: gypsum dissolves rapidly while bassanite dissolves slowly. This difference in dissolution rates may explain why secondary gypsum crystals exhibit a higher degree of mesoscale ordering compared to the initial crystals (Fig. 6). Namely, the gradual increase in saturation in the presence of an interface (i.e. dissolving bassanite crystals) would promote the formation of fewer nuclei, slower growth, and consequently, larger and better-ordered gypsum crystals, which aligns with our observations. When gypsum became the dominant phase, the sulfate concentration increased slightly, and with only gypsum remaining, the concentration of sulfate equilibrated at ~41 mM. When the same solution was heated again to T = 90 °C, a very similar trend in the sulfate concentration profile as the one observed during the first heating stage was observed (Fig. 2B).

In Fig. 8C, we compare the experimental solubility values of gypsum and bassanite in a 4.8 M NaCl brine at different temperatures, as extracted from the Raman spectra, with the solubility curves calculated using PHREEQC 3 (see also Fig. 1C). This graph reveals a notable discrepancy between the theoretical curves and the experimental data. At room temperature, the measured solubilities of gypsum and, especially, bassanite are lower than the calculated ones. This finding is remarkable because solubility measured from precipitation experiments typically overestimates the actual solubility due to the time required to reach true equilibrium. Noteworthy, when the temperature is rapidly increased to T = 90 °C, the observed increase in free sulfate concentration in the solution contradicts expectations, as it was commonly assumed that the solubility of gypsum significantly decreases with rising temperatures under low salinity conditions(Van Driessche et al., 2019). However, the revised PHREEQC 3 code predicts this increase in gypsum solubility with temperature for highly saline solutions. Overall, numerical solubility predictions in brines are (still) not accurate enough to determine the phase stability in the $CaSO_4$ system and more experimental data is required for different conditions and salts. For instance, it was reported by Ding et al. that in NH_4Cl brines at elevated temperatures gypsum is fully soluble into stable ions (Ding et al., 2023), presenting a more extreme case compared to what happens in NaCl.

3.4. Towards a sustainable bassanite synthesis

The cyclic transformations of gypsum-to-bassanite in high-salinity brines offer an efficient route to produce hemihydrate. To demonstrate the practicality of this method, we also processed natural gypsum into bassanite. We used 0.2 M $CaSO_4$ equivalent solutions/slurries, containing 34.4 g/L of dispersed natural gypsum powder (see SI: Materials and Methods). We reproduced the processes at high salinity with 4.8 M NaCl brines. A detailed plot of the Raman spectra in the first 60000 s after raising the temperature to T = 90 °C shows, as expected, the evolution of the transformation of gypsum to bassanite and back to gypsum (SI: Fig. S7). After raising the temperature, gypsum completely transformed into bassanite within 1500 s and that the hemihydrate remained stable for >30000 s after the temperature was lowered to T = 35 °C, until gypsum eventually reprecipitated.

Building upon these ideas and observations with natural gypsum, we further explored the scenario in which the salinity would be substantially lower. We highlight here the experiment performed at 0.2 M $CaSO_4$ and 0.4 M NaCl (SI: Fig. S8). Compared to the high salinity experiment (4.8 M NaCl), the low salinity one showed three significant differences. Firstly, a much higher temperature, T > 115 °C, was required to facilitate the rapid transformation of gypsum to bassanite (SI: Fig. S8A). Secondly, during this transformation, there was no increase in the sulfate concentration; instead, it sharply dropped (SI: Fig. S8B). Thirdly, the conversion of bassanite to gypsum happened much faster when the temperature was lowered to T = 35 °C. Notably, at the beginning of the transformation from bassanite to gypsum, there was a peak in sulfate concentration (SI: Fig. S8B), similar to what was

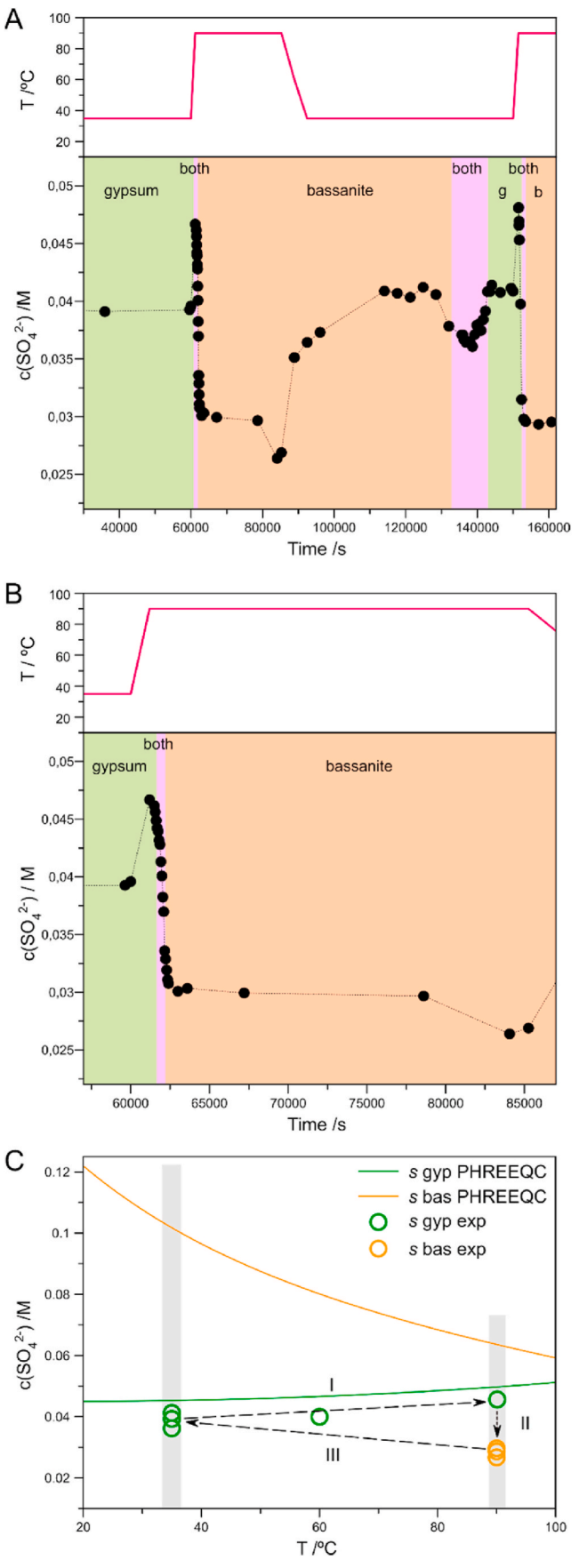

(caption on next column)

Fig. 8. Aqueous sulfate concentration evolution during gypsum-bassanite-gypsum conversion. (A) 2 cycles of gypsum to bassanite conversion when heating the solution at 35 °C < T < 90 °C. (B) Detail of the first gypsum to bassanite cycle shown in (A). The red dotted curve indicates the temperature profile. The coloured backgrounds mark the phase occurrence regions: gypsum (green), bassanite (orange); both phases (purple). (C) Theoretical solubility curves of gypsum (green curve) and bassanite (orange curve) as a function of temperature. Experimental measured concentration (exp) of aqueous sulfate at an apparent equilibrium with a solid phase (green dot = gypsum, orange dot = bassanite). Black arrows indicate the peak in aqueous sulfate concentration at the onset of gypsum to of bassanite transformation. (For interpretation of the references to colour in this figure legend, the reader is referred to the Web version of this article.)

observed in the inverse reaction in the high salinity experiment.

The first two differences can be explained by considering the changing trends in the solubility curves of gypsum and bassanite as a function of salinity, as illustrated in Fig. 1 and SI: Fig. S9A. Using PHREEQC 3, calculations predict a crossover temperature between gypsum and bassanite solubilities at 0.4 M NaCl and ~106 °C. However, experimental solubility data obtained by measuring sulfate concentrations in solutions containing 0.4 M and 4.8 M NaCl in contact with gypsum or bassanite at different temperatures (as shown in SI: Figs. S9B and SI: S9C) indicate that the solubility crossover occurs at a much lower temperature than predicted in the case of 4.8 M NaCl. This discrepancy is mainly because the calculated solubility of bassanite is much higher than the measured one at high salinity. In contrast, the experimental and calculated solubility values compare better for low salinity, although the experimental values are lower than the predicted ones. The increase in sulfate concentration with increasing temperature, during the high salinity experiment can be attributed to an increase in gypsum solubility, as evidenced by the trend in both calculated and experimental data. Lastly, the fast transformation from bassanite to gypsum at low salinity can also be attributed to the shift in the solubility crossover.

To establish the critical salt concentration for a rapid gypsum to bassanite transformation (assuming, arbitrarily, <1 h to be a practical threshold), a series of experiments at different salt concentrations were carried out at T = 90 °C using unstirred batch reactors. These experiments revealed that a NaCl concentration of >4 M is needed to induce rapid (<1 h) transformation times (SI: Table S3). At lower salt concentrations, such as 1.4 M NaCl, the transformation rate is significantly reduced, with gypsum not transforming to bassanite even after 11 days. Additionally, the critical temperature for a rapid gypsum-to-bassanite transformation was established at 4.8 M NaCl. Table S2 in SI, shows that only at T = 90 °C, the transformation is fast (<1 h) in unstirred reactors. Experiments conducted at T = 70 °C indicate that it takes up to 5 days to transform gypsum to bassanite, which from an industrial perspective is not interesting. But it does confirm again that in high salinity solutions, the solubility crossover is shifted to much lower temperatures than those predicted by the thermodynamic calculations. We must add here that increasing salinity and temperature is likely to have also a possible adverse effect, in which Na^+ is more readily incorporated into a bassanite structure(Mees et al., 2008; Reigl et al., 2022; Ru et al., 2012). At very high NaCl concentrations, this could potentially lead to the formation of inclusions of e.g., glauberite ($Na_2Ca(SO_4)_2$)(Araki and Zoltai, 1967) or omongwaite ($Na_2Ca_5(SO_4)_6{\cdot}3H_2O$) (Mees et al., 2008; Ru et al., 2012). However, the primary impact of NaCl is to induce non-specific ion effects, such as changes in net ionic strength. These changes affect the activity coefficients of all ions, including water, and most importantly the relative solubilities of the different phases.

At the crystallographic level, gypsum readily and rapidly converts to bassanite in solution, making different sources of gypsum potentially useable. Meanwhile, the fate of various contaminants in waste gypsum during processing remains an ongoing research focus for numerous groups worldwide(Bouargane et al., 2023; Guan et al., 2009a, 2023;

Haneklaus et al., 2022; Ru et al., 2012; Rutherford et al., 1994). Solution-driven processing offers significantly more control over the gypsum conversion/dehydration processes compared to solid-state methods. The dissolution of gypsum, and its impurities, into ions presents the opportunity to scavenge these impurities using for example complexing agents.

4. Conclusions

The considered solution-driven calcium sulfate processing in brines is an efficient method to make bassanite. In this regard, the optimum conditions to obtain bassanite in a short time (<1 h, in practice several minutes) involve brines c(NaCl) > 4 M, and T > 80 °C. The fact that the transformations are solution-driven opens extensive possibilities of well-controlled crystal engineering. We demonstrated that bassanite remains present as the only crystalline phase for an extended period of time, before it converts to gypsum. This is a highly beneficial aspect for practical processing and harvesting of crystals under industrial scenarios. Furthermore, the complexity of transformation pathways at the nanoscale, as depicted in Fig. 7, suggests the possibility of developing additives and processing strategies that can target specific stages of these processes. For instance, they could either enhance or prevent the occurrence of the mesostructural disorder in the crystals, which would result in materials of different surface areas and reactivities(Guan et al., 2009b, 2010, 2021, 2023).

CRediT authorship contribution statement

Tomasz M. Stawski: Conceptualization, Data curation, Formal analysis, Funding acquisition, Investigation, Methodology, Project administration, Resources, Software, Supervision, Validation, Visualization, Writing – original draft, Writing – review & editing. **Stephanos Karafiludis:** Formal analysis, Investigation, Validation, Writing – review & editing, Methodology, Writing – original draft, Data curation. **Carlos Pimentel:** Formal analysis, Investigation, Writing – review & editing, Data curation, Methodology, Writing – original draft. **German Montes-Hernández:** Investigation. **Zdravko Kochovski:** Investigation. **Ralf Bienert:** Investigation. **Karin Weimann:** Investigation. **Franziska Emmerling:** Investigation, Resources. **Ernesto Scoppola:** Formal analysis, Investigation, Methodology, Software, Writing – review & editing, Data curation. **Alexander E.S. Van Driessche:** Conceptualization, Data curation, Formal analysis, Funding acquisition, Investigation, Methodology, Project administration, Resources, Supervision, Validation, Visualization, Writing – original draft, Writing – review & editing.

Declaration of competing interest

The authors declare that they have no known competing financial interests or personal relationships that could have appeared to influence the work reported in this paper.

Data availability

Data will be made available on request.

Acknowledgements

We thank BAM (project MIT1-20-09) and Helmholtz-Zentrum Berlin (HZB) for providing us with the beamtime at mySpot of BESSY II (proposal 211-10162-ST-1.1-P) and access to electron microscopes. AESVD acknowledges funding from the Junta de Andalucia (Spain) through project PROYEXCEL_00771. CP has received funding from the European Union's Horizon 2020 research and innovation programme under the Marie Sklodowska-Curie grant agreement No. 101021894 [CARS-CO2].

Appendix A. Supplementary data

Supplementary data to this article can be found online at https://doi.org/10.1016/j.jclepro.2024.141012.

References

Aagli, A., Tamer, N., Atbir, A., Boukbir, L., El Hadek, M., 2005. Conversion of phosphogypsum to potassium sulfate. J. Therm. Anal. Calorim. 82, 395–399. https://doi.org/10.1007/s10973-005-0908-y.

Alyousef, R., Abbass, W., Aslam, F., Shah, M.I., 2023. Potential of waste woven polypropylene fiber and textile mesh for production of gypsum-based composite. Case Stud. Constr. Mater. 18, e02099 https://doi.org/10.1016/j.cscm.2023.e02099.

Araki, T., Zoltai, T., 1967. Refinement of the crystal structure of a glauberite. Am. Mineral. 52, 1272–1277.

Ash, S., 2019. Mineral Commodity Summaries 2019. US Geological Survey Reston, VA.

Besselink, R., Stawski, T.M., Van Driessche, A.E.S., Benning, L.G., 2016. Not just fractal surfaces, but surface fractal aggregates: Derivation of the expression for the structure factor and its applications. J. Chem. Phys. 145, 211908 https://doi.org/10.1063/1.4960953.

Bezou, C., Nonat, A., Mutin, J.-C., Christensen, A.N., Lehmann, M.S., 1995. Investigation of the crystal structure of γ-CaSO4, CaSO4 · 0.5 H2O, and CaSO4 · 0.6 H2O by powder diffraction methods. J. Solid State Chem. 117, 165–176. https://doi.org/10.1006/jssc.1995.1260.

Bouargane, B., Laaboubi, K., Biyoune, M.G., Bakiz, B., Atbir, A., 2023. Effective and innovative procedures to use phosphogypsum waste in different application domains: review of the environmental, economic challenges and life cycle assessment. J. Mater. Cycles Waste Manag. 25, 1288–1308. https://doi.org/10.1007/s10163-023-01617-8.

Bučar, D.-K., Lancaster, R.W., Bernstein, J., 2015. Disappearing polymorphs revisited. Angew. Chem. Int. Ed. 54, 6972–6993. https://doi.org/10.1002/anie.201410356.

Buchert, M., Sutter, J., Alwas, H., 2017. Ökobilanzielle Betrachtung des Recyclings von Gipskartonplatten. Endbericht. Dessau-Roßlau Umweltbundesamt UBA-Texte 33 110.

Burgos-Ruiz, M., Pelayo-Punzano, G., Ruiz-Agudo, E., Elert, K., Rodriguez-Navarro, C., 2021. Synthesis of high surface area CaSO4·0.5H2O nanorods using calcium ethoxide as precursor. Chem. Commun. 57, 7304–7307. https://doi.org/10.1039/D1CC02014E.

Conti, M., Meerson, B., Peleg, A., Sasorov, P.V., 2002. Phase ordering with a global conservation law: Ostwald ripening and coalescence. Phys. Rev. E 65, 046117.

Ding, W., Qiao, J., Zeng, L., Sun, H., Peng, T., 2023. Desulfurization gypsum carbonation for CO2 sequestration by using recyclable ammonium salt. Int. J. Greenh. Gas Control 123, 103843. https://doi.org/10.1016/j.ijggc.2023.103843.

Dunitz, J.D., Bernstein, J., 1995. Disappearing polymorphs. Acc. Chem. Res. 28, 193–200.

European Commission. Gypsum industry news from global gypsum [WWW Document], n.d. URL. https://www.globalgypsum.com/news/itemlist/tag/European%20Commission, 7.18.23.

Feldmann, T., Demopoulos, G.P., 2013. Influence of impurities on crystallization kinetics of calcium sulfate dihydrate and hemihydrate in Strong HCl-CaCl2 solutions. Ind. Eng. Chem. Res. 52, 6540–6549. https://doi.org/10.1021/ie302933v.

Fu, H., Guan, B., Jiang, G., Yates, M.Z., Wu, Z., 2012. Effect of supersaturation on competitive nucleation of CaSO4 phases in a concentrated CaCl2 solution. Cryst. Growth Des. 12, 1388–1394.

Guan, B., Jiang, G., Wu, Z., Mao, J., Kong, B., 2011. Preparation of α-calcium sulfate hemihydrate from calcium sulfate dihydrate in methanol–water solution under mild conditions. J. Am. Ceram. Soc. 94, 3261–3266. https://doi.org/10.1111/j.1551-2916.2011.04470.x.

Guan, B., Yang, L., Wu, Z., 2010. Effect of Mg2+ ions on the nucleation kinetics of calcium sulfate in concentrated calcium chloride solutions. Ind. Eng. Chem. Res. 49, 5569–5574. https://doi.org/10.1021/ie902022b.

Guan, B., Yang, L., Wu, Z., Shen, Z., Ma, X., Ye, Q., 2009a. Preparation of α-calcium sulfate hemihydrate from FGD gypsum in K, Mg-containing concentrated CaCl2 solution under mild conditions. Fuel, Selected Papers from the 2007 World of Coal Ash Conference 88, 1286–1293. https://doi.org/10.1016/j.fuel.2009.01.004.

Guan, B., Yang, L., Wu, Z., Shen, Z., Ma, X., Ye, Q., 2009b. Preparation of α-calcium sulfate hemihydrate from FGD gypsum in K, Mg-containing concentrated CaCl2 solution under mild conditions. Fuel, Selected Papers from the 2007 World of Coal Ash Conference 88, 1286–1293. https://doi.org/10.1016/j.fuel.2009.01.004.

Guan, Q., Sui, Y., Zhang, F., Yu, W., Bo, Y., Wang, P., Peng, W., Jin, J., 2021. Preparation of α-calcium sulfate hemihydrate from industrial by-product gypsum: a review. Physicochem. Probl. Miner. Process. 57, 168–181.

Guan, Q., Zhou, Y., Yu, W., Fan, R., Sui, Y., Bu, Y., Yin, Z., Chi, R., Gao, Z., 2023. Efficient removal of impurities from phosphogypsum during preparation of α-hemihydrate gypsum. Miner. Eng. 201, 108203 https://doi.org/10.1016/j.mineng.2023.108203.

Gürtürk, M., Oztop, H.F., 2016. Exergoeconomic analysis of a rotary kiln used for plaster production as building materials. Appl. Therm. Eng. 104, 486–496. https://doi.org/10.1016/j.applthermaleng.2016.05.106.

Haneklaus, N., Barbossa, S., Basallote, M.D., Bertau, M., Bilal, E., Chajduk, E., Chernysh, Y., Chubur, V., Cruz, J., Dziarczykowski, K., Fröhlich, P., Grosseau, P., Mazouz, H., Kiegiel, K., Nieto, J.M., Pavón, S., Pessanha, S., Pryzowicz, A., Roubík, H., Cánovas, C.R., Schmidt, H., Seeling, R., Zakrzewska-Kołtuniewicz, G., 2022. Closing the upcoming EU gypsum gap with phosphogypsum. Resour. Conserv. Recycl. 182, 106328 https://doi.org/10.1016/j.resconrec.2022.106328.

He, S., Oddo, J.E., Tomson, M.B., 1994. The nucleation kinetics of calcium sulfate dihydrate in NaCl solutions up to 6 m and 90 C. J. Colloid Interface Sci. 162, 297–303.

Herrero, M.J., Escavy, J.I., Bustillo, M., 2013. The Spanish building crisis and its effect in the gypsum quarry production (1998–2012). Resour. Pol. 38, 123–129. https://doi.org/10.1016/j.resourpol.2013.02.005.

Karafiludis, S., Scoppola, E., Wolf, S.E., Kochovski, Z., Matzdorff, D., Driessche, A.E.S.V., Hövelmann, J., Emmerling, F., Stawski, T.M., 2023. Evidence for Liquid-Liquid Phase Separation during the Early Stages of Mg-Struvite Formation. https://doi.org/10.26434/chemrxiv-2023-6k339.

La Bella, M., Besselink, R., Wright, J.P., Van Driessche, A.E.S., Fernandez-Martinez, A., Giacobbe, C., 2023. Hierarchical synchrotron diffraction and imaging study of the calcium sulfate hemihydrate-gypsum transformation. J. Appl. Crystallogr. 56, 660–672. https://doi.org/10.1107/S1600576723002881.

López-Delgado, A., López-Andrés, S., Padilla, I., Alvarez, M., Galindo, R., Vázquez, A.J., 2014. Dehydration of gypsum rock by solar energy: preliminary study. Geomaterials 2014. https://doi.org/10.4236/gm.2014.43009.

Maslyk, M., Dallos, Z., Koziol, M., Seiffert, S., Hieke, T., Petrović, K., Kolb, U., Mondeshki, M., Tremel, W., 2022. A fast and sustainable route to bassanite nanocrystals from gypsum. Adv. Funct. Mater. 32, 2111852 https://doi.org/10.1002/adfm.202111852.

Mees, F., Hatert, F., Rowe, R., 2008. Omongwaite, Na2Ca5(SO4)6.3H2O, a new mineral from recent salt lake deposits, Namibia. Mineral. Mag. 72, 1307–1318. https://doi.org/10.1180/minmag.2008.072.6.1307.

Montes-Hernandez, G., Renard, F., 2016. Time-resolved in situ Raman spectroscopy of the nucleation and growth of siderite, magnesite, and calcite and their precursors. Cryst. Growth Des. 16, 7218–7230. https://doi.org/10.1021/acs.cgd.6b01406.

Nie, Z., Wei, Z., Yang, Y., Guo, X., Chang, Y., Yi, G., 2023. Facile preparation of large-sized columnar α-HH crystal via a NaCl salt bath method. Cryst. Res. Technol. 58, 2200278 https://doi.org/10.1002/crat.202200278.

Ossorio, M., Van Driessche, A.E.S., Pérez, P., García-Ruiz, J.M., 2014. The gypsum–anhydrite paradox revisited. Chem. Geol. 386, 16–21. https://doi.org/10.1016/j.chemgeo.2014.07.026.

Parkhurst, D.L., Appelo, C., 2013. Description of input and examples for PHREEQC version 3—a computer program for speciation, batch-reaction, one-dimensional transport, and inverse geochemical calculations. US Geol. Surv. Tech. Methods 6, 497.

Parkhurst, D.L., Appelo, C., 1999. User's guide to PHREEQC (Version 2): a computer program for speciation, batch-reaction, one-dimensional transport, and inverse geochemical calculations. Water-Resour. Investig. Rep. 99, 312.

Powell, D.A., 1962. Calcium sulphate hemihydrate prepared in sodium chloride solution. Aust. J. Chem. 15, 868–873. https://doi.org/10.1071/ch9620868.

Reigl, S., Driessche, A.E.S.V., Mehringer, J., Koltzenburg, S., Kunz, W., Kellermeier, M., 2022. Revisiting the roles of salinity, temperature and water activity in phase selection during calcium sulfate precipitation. CrystEngComm 24, 1529–1536. https://doi.org/10.1039/D1CE01664D.

Reigl, S., Driessche, A.E.S.V., Ullrich, T., Koltzenburg, S., Kunz, W., Kellermeier, M., 2023a. Organic solvent-free synthesis of calcium sulfate hemihydrate at room temperature. Chem. Commun. https://doi.org/10.1039/D3CC02552G.

Reigl, S., Van Driessche, A.E.S., Wagner, E., Montes-Hernandez, G., Mehringer, J., Koltzenburg, S., Kunz, W., Kellermeier, M., 2023b. Toward more sustainable hydraulic binders: controlling calcium sulfate phase selection via specific additives. ACS Sustain. Chem. Eng. https://doi.org/10.1021/acssuschemeng.3c00429.

Reiss, A.G., Gavrieli, I., Rosenberg, Y.O., Reznik, I.J., Luttge, A., Emmanuel, S., Ganor, J., 2021. Gypsum precipitation under saline conditions: thermodynamics, kinetics, morphology, and size distribution. Minerals 11, 141. https://doi.org/10.3390/min11020141.

Ru, X., Ma, B., Huang, J., Huang, Y., 2012. Phosphogypsum transition to α-calcium sulfate hemihydrate in the presence of omongwaite in NaCl solutions under atmospheric pressure. J. Am. Ceram. Soc. 95, 3478–3482. https://doi.org/10.1111/j.1551-2916.2012.05429.x.

Rutherford, P.M., Dudas, M.J., Samek, R.A., 1994. Environmental impacts of phosphogypsum. Sci. Total Environ. 149, 1–38. https://doi.org/10.1016/0048-9697(94)90002-7.

Saha, A., Lee, J., Pancera, S.M., Bräeu, M.F., Kempter, A., Tripathi, A., Bose, A., 2012. New Insights into the transformation of calcium sulfate hemihydrate to gypsum using time-resolved cryogenic transmission electron microscopy. Langmuir 28, 11182–11187.

Salman, O.A., Khraishi, N., 1988. Thermal decomposition of limestone and gypsum by solar energy. Sol. Energy 41, 305–308. https://doi.org/10.1016/0038-092X(88)90025-4.

Schmid, T., Jungnickel, R., Dariz, P., 2020. Insights into the CaSO4–H2O system: a Raman-spectroscopic study. Minerals 10, 115. https://doi.org/10.3390/min10020115.

Shen, L., Sippola, H., Li, X., Lindberg, D., Taskinen, P., 2020. Thermodynamic modeling of calcium sulfate hydrates in a CaSO4–H2SO4–H2O system from 273.15 to 473.15 K up to 5 m sulfuric acid. J. Chem. Eng. Data 65, 2310–2324. https://doi.org/10.1021/acs.jced.9b00829.

Singh, N.B., Middendorf, B., 2007a. Calcium sulphate hemihydrate hydration leading to gypsum crystallization. Prog. Cryst. Growth Char. Mater. 53, 57–77. https://doi.org/10.1016/j.pcrysgrow.2007.01.002.

Singh, N.B., Middendorf, B., 2007b. Calcium sulphate hemihydrate hydration leading to gypsum crystallization. Prog. Cryst. Growth Char. Mater. 53, 57–77. https://doi.org/10.1016/j.pcrysgrow.2007.01.002.

Stawski, T.M., Besselink, R., Chatzipanagis, K., Hövelmann, J., Benning, L.G., Van Driessche, A.E.S., 2020. Nucleation pathway of calcium sulfate hemihydrate (bassanite) from solution: implications for calcium sulfates on mars. J. Phys. Chem. C 124, 8411–8422. https://doi.org/10.1021/acs.jpcc.0c01041.

Stawski, T.M., Freeman, H.M., Van Driessche, A.E.S., Hövelmann, J., Besselink, R., Wirth, R., Benning, L.G., 2019. Particle-mediated nucleation pathways are imprinted in the internal structure of calcium sulfate single crystals. Cryst. Growth Des. 19, 3714–3721. https://doi.org/10.1021/acs.cgd.9b00066.

Stawski, T.M., Smales, G.J., Scoppola, E., Jha, D., Morales, L.F.G., Moya, A., Wirth, R., Pauw, B.R., Emmerling, F., Van Driessche, A.E.S., 2021. Seeds of imperfection rule the mesocrystalline disorder in natural anhydrite single crystals. Proc. Natl. Acad. Sci. USA 118, e2111213118. https://doi.org/10.1073/pnas.2111213118.

Stawski, T.M., Van Driessche, A.E.S., Ossorio, M., Diego Rodriguez-Blanco, J., Besselink, R., Benning, L.G., 2016. Formation of calcium sulfate through the aggregation of sub-3 nanometre primary species. Nat. Commun. 7, 11177 https://doi.org/10.1038/ncomms11177.

Tritschler, U., Kellermeier, M., Debus, C., Kempter, A., Cölfen, H., 2015a. A simple strategy for the synthesis of well-defined bassanite nanorods. CrystEngComm 17, 3772–3776. https://doi.org/10.1039/C5CE00519A.

Tritschler, U., Kellermeier, M., Debus, C., Kempter, A., Cölfen, H., 2015b. A simple strategy for the synthesis of well-defined bassanite nanorods. CrystEngComm 17, 3772–3776. https://doi.org/10.1039/c5ce00519a.

Van Driessche, A.E.S., Stawski, T.M., Kellermeier, M., 2019. Calcium sulfate precipitation pathways in natural and engineered environments. Chem. Geol. 530, 119274 https://doi.org/10.1016/j.chemgeo.2019.119274.

Weimann, K., Adam, C., Buchert, M., Sutter, J., 2021. Environmental evaluation of gypsum plasterboard recycling. Minerals 11, 101. https://doi.org/10.3390/min11020101.

Weiss, H., Bräu, M.F., 2009. How much water does calcined gypsum contain? Angew. Chem. Int. Ed. 48, 3520–3524. https://doi.org/10.1002/anie.200900726.

Zürz, A., Odler, I., Thiemann, F., Berghöfer, K., 1991. Autoclave-free Formation of α-hemihydrate gypsum. J. Am. Ceram. Soc. 74, 1117–1124. https://doi.org/10.1111/j.1151-2916.1991.tb04351.x.